Title

Ultrahigh-resolution optical coherence tomography with monochromatic and chromatic aberration correction.

Journal

Optics express, 16(11)

ISSN

1094-4087

Authors

Zawadzki, Robert J
Cense, Barry
Zhang, Yan
et al.

Publication Date

2008-05-01

DOI

10.1364/oe.16.008126

Peer reviewed

Ultrahigh-resolution optical coherence tomography with monochromatic and chromatic aberration correction

Robert J. Zawadzki,[1,*] Barry Cense,[2] Yan Zhang,[2,3] Stacey S. Choi,[1] Donald T. Miller,[2] and John S. Werner[1]

[1]*Vision Science and Advanced Retinal Imaging Laboratory (VSRI), Dept. of Ophthalmology & Vision Science UC Davis, 4860 Y Street, Suite 2400, Sacramento, CA 95817, USA*

[2]*School of Optometry, Indiana University, 800 E. Atwater Ave., Bloomington, IN 47405,USA*

[3]*Currently with the Alcon Laboratories, Inc., Ft. Worth, Texas 76134, USA*

[*]*Corresponding author: rjzawadzki@ucdavis.edu*

Abstract: We have developed an improved adaptive optics - optical coherence tomography (AO-OCT) system and evaluated its performance for in vivo imaging of normal and pathologic retina. The instrument provides unprecedented image quality at the retina with isotropic 3D resolution of 3.5 x 3.5 x 3.5 μm^3. Critical to the instrument's resolution is a customized achromatizing lens that corrects for the eye's longitudinal chromatic aberration and an ultra broadband light source ($\Delta\lambda$=112nm λ_0=~836 nm). The eye's transverse chromatic aberrations is modeled and predicted to be sufficiently small for the imaging conditions considered. The achromatizing lens was strategically placed at the light input of the AO-OCT sample arm. This location simplifies use of the achromatizing lens and allows straightforward implementation into existing OCT systems. Lateral resolution was achieved with an AO system that cascades two wavefront correctors, a large stroke bimorph deformable mirror (DM) and a micro-electromechanical system (MEMS) DM with a high number of actuators. This combination yielded diffraction-limited imaging in the eyes examined. An added benefit of the broadband light source is the reduction of speckle size in the axial dimension. Additionally, speckle contrast was reduced by averaging multiple B-scans of the same proximal patch of retina. The combination of improved micron-scale 3D resolution, and reduced speckle size and contrast were found to significantly improve visibility of microscopic structures in the retina.

OCIS codes: (110.4500) Optical coherence tomography; (010.1080) Adaptive optics; (220.1000) Aberration compensation; (170.0110) imaging system; (170.4470) ophthalmology; (120.3890) Medical optics instrumentation

References and links

1. D. Huang, E. A. Swanson, C. P. Lin, J. S. Schuman, W. G. Stinson, W. Chang, M. R. Flotte, K. Gregory, and C. A. Puliafito, "Optical coherence tomography," Science **254**, 1178-1181 (1991).
2. A. F. Fercher, C. K. Hitzenberger, G. Kamp, and Y. Elzaiat, "Measurement of intraocular distances by backscattering spectral interferometry," Opt. Commun. **117**, 43-48 (1995).
3. M. Wojtkowski, R. Leitgeb, A. Kowalczyk, T. Bajraszewski, and A. F. Fercher, "In vivo human retinal imaging by fourier domain optical coherence tomography," J. Biomed. Opt. **7**, 457-463 (2002).
4. N. A. Nassif, B. Cense, B. H. Park, M. C. Pierce, S. H. Yun, B. E. Bouma, G. J. Tearney, T. C. Chen, and J. F. de Boer, "In vivo high-resolution video-rate spectral-domain optical coherence tomography of the human retina and optic nerve," Opt. Express **12**, 367-376 (2004).
5. M. Wojtkowski, V. Srinivasan, J. Fujimoto, T. Ko, J. Schuman, A. Kowalczyk, and J. Duker, "Three-dimensional retinal imaging with high-speed ultrahigh-resolution optical coherence tomography," Ophthalmology, **112**, 1734-1746 (2005).

#94149 - $15.00 USD Received 24 Mar 2008; revised 16 May 2008; accepted 17 May 2008; published 20 May 2008

6. S. Alam, R. J. Zawadzki, S. S. Choi, C. Gerth, S. S. Park, L. Morse, and J. S. Werner, "Clinical application of rapid serial Fourier-domain optical coherence tomography for macular imaging," Ophthalmology **113**, 1425-1431 (2006).
7. S. N. Truong, S. Alam, R. J. Zawadzki, S. S. Choi, D. G. Telander, S. S. Park, J. S. Werner and L. S. Morse, "High-resolution Fourier-domain optical coherence tomography of retinal angiomatous proliferation," Retina **27**, 915-925 (2007).
8. W. Drexler and J. G. Fujimoto, "Optical coherence tomography in ophthalmology" J. Biomed. Opt. **12**, 041201 (2007).
9. W. J. Donnelly III and A. Roorda, "Optimal pupil size in the human eye for axial resolution," J. Opt. Soc. Am. A **20**, 2010-2015 (2003), http://www.opticsinfobase.org/abstract.cfm?URI=josaa-20-11-2010.
10. J. Liang, D. R. Williams and D. T. Miller, "Supernormal vision and high-resolution retinal imaging through adaptive optics," J. Opt. Soc. Am. A **14**, 2884 (1997), http://www.opticsinfobase.org/abstract.cfm?URI=josaa-14-11-2884.
11. A. Roorda, F. Romero-Borja, W. J. Donnelly III, H. Queener, T. J. Hebert, and M. C. W. Campbell, "Adaptive optics scanning laser ophthalmoscopy," Opt. Express **10**, 405-412 (2002).
12. D. T. Miller, J. Qu, R. S. Jonnal, and K. Thorn, "Coherence gating and adaptive optics in the eye," Proc. SPIE **4956**, 65-72 (2003).
13. B. Hermann, E. J. Fernandez, A. Unterhubner, H. Sattmann, A. F. Fercher, and W. Drexler, P. M. Prieto and P. Artal, "Adaptive-optics ultrahigh-resolution optical coherence tomography," Opt. Lett. **29**, 2142-2144 (2004).
14. D. Merino, C. Dainty, A. Bradu, and A. G. Podoleanu, "Adaptive optics enhanced simultaneous en-face optical coherence tomography and scanning laser ophthalmoscopy," Opt. Express **14**, 3345-3353 (2006).
15. Y. Zhang, J. Rha, R. S. Jonnal, D. T. Miller, "Adaptive optics parallel spectral domain optical coherence tomography for imaging the living retina," Opt. Express **13**, 4792-4811 (2005).
16. R. J. Zawadzki, S. M. Jones, S. S. Olivier, M. Zhao, B. A. Bower, J. A. Izatt, S. Choi, S. Laut, and J. S. Werner, "Adaptive-optics optical coherence tomography for high-resolution and high-speed 3D retinal in vivo imaging," Opt. Express **13**, 8532-8546 (2005).
17. Y. Zhang, B. Cense, J. Rha, R. S. Jonnal, W. Gao, R. J. Zawadzki, J. S. Werner, S. Jones, S. Olivier, and D. T. Miller, "High-speed volumetric imaging of cone photoreceptors with adaptive optics spectral-domain optical coherence tomography," Opt. Express **14**, 4380-4394 (2006).
18. E. Fernández, B. Povazay, B. Hermann, A. Unterhuber, H. Sattman, P. Prieto, R. Leitgeb, P. Anhelt, P. Artal, W. Drexler, "Three-dimensional adaptive optics ultrahigh-resolution optical coherence tomography using liquid crystal spatial light modulator," Vision. Res. **45**, 3432-3444 (2005).
19. R. J. Zawadzki, S. S. Choi, S. M. Jones, S. S. Olivier, J. S. Werner, "Adaptive optics - optical coherence tomography: optimizing visualization of microscopic retinal structures in three dimensions." J. Opt. Soc. Am. A **24**, 1373-1383 (2007).
20. C. E. Bigelow, N. V. Iftimia, R. D. Ferguson, T. E. Ustun, B. Bloom, and D. X. Hammer, "Compact multimodal adaptive-optics spectral-domain optical coherence tomography instrument for retinal imaging," J. Opt. Soc. Am. A **24**, 1327-1336 (2007), http://www.opticsinfobase.org/abstract.cfm?URI=josaa-24-5-1327.
21. M. Pircher, R. J. Zawadzki, J. W. Evans, J. S. Werner and C. K. Hitzenberger, "Simultaneous imaging of human cone mosaic with adaptive optics enhanced scanning laser ophthalmoscopy and high- speed transversal scanning optical coherence tomography," Opt. Lett. **33**, 22-24 (2008), http://www.opticsinfobase.org/abstract.cfm?URI=oe-10-9-405.
22. M. Pircher and R. J. Zawadzki, "Combining adaptive optics with optical coherence tomography: Unveiling the cellular structure of the human retina in vivo," Expert Review of Ophthalmology **2**, 1019-1035 (2007).
23. W. Drexler, U. Morgner, R. K. Ghanta, F. X. Kartner, J. S. Schuman, and J. G. Fujimoto, "Ultrahigh-resolution ophthalmic optical coherence tomography," Nat. Med. **7**, 502-507 (2001).
24. J. F. de Boer, B. Cense, B. H. Park, M. C. Pierce, G. J. Tearney, and B. E. Bouma, "Improved signal-to-noise ratio in spectral-domain compared with time-domain optical coherence tomography," Opt. Lett. **28**, 2067-2069 (2003), http://www.opticsinfobase.org/abstract.cfm?URI=ol-28-21-2067.
25. R. Leitgeb, C. K. Hitzenberger, and A. F. Fercher, "Performance of fourier domain vs. time domain optical coherence tomography," Opt. Express **11**, 889-894 (2003).
26. B. Cense, N. A. Nassif, T. C. Chen, M. C. Pierce, S. H. Yun, B. H. Park, B. E. Bouma, G. J. Tearney, and J. F. de Boer, "Ultrahigh-resolution high-speed retinal imaging using spectral-domain optical coherence tomography," Opt. Express **12**, 2435-2447 (2004).
27. M. Wojtkowski, V. J. Srinivasan, T. H. Ko, J.G. Fujimoto, A. Kowalczyk, and J. S. Duker, "Ultrahigh-resolution, high-speed, Fourier domain optical coherence tomography and methods for dispersion compensation," Opt. Express **12**, 2404-2422 (2004).
28. T. M. Jørgensen, J. Thomadsen, U. Christensen, W. Soliman, and B. Sander, "Enhancing the signal-to-noise ratio in ophthalmic optical coherence tomography by image registration—method and clinical examples" J. Biomed. Opt. **12**, 041208 (2007).
29. D. A. Atchison and G. Smith, *Optics of the Human Eye* (Butterworth-Heinemann, 2000).
30. E. J. Fernández, A. Unterhuber, P. M. Prieto, B. Hermann, W. Drexler, and P. Artal, "Ocular aberrations as a function of wavelength in the near infrared measured with a femtosecond laser," Opt. Express **13**, 400-409 (2005).
31. E. J. Fernández, A. Unterhuber, B. Považay, B. Hermann, P. Artal, and W. Drexler, "Chromatic aberration correction of the human eye for retinal imaging in the near infrared," Opt. Express **14**, 6213-6225 (2006).

#94149 - $15.00 USD Received 24 Mar 2008; revised 16 May 2008; accepted 17 May 2008; published 20 May 2008

32. D. A. Atchison and G. Smith, "Chromatic dispersions of the ocular media of human eyes," J. Opt. Soc. Am. A **22**, 29-37 (2005), http://www.opticsinfobase.org/abstract.cfm?URI=josaa-22-1-29.
33. A. C. van Heel, "Correcting the spherical and chromatic aberrations of the eye," J. Opt. Soc. Am. **36**, 237-239 (1947).
34. R. E. Bedford and G. Wyszecki, "Axial chromatic aberration of the human eye," J. Opt. Soc. Am. **47**, 564-565 (1957).
35. A. L. Lewis, M. Katz, and C. Oehrlein, "A modified achromatizing lens," Am. J. Optom. Physiol. Opt. **59**, 909-911 (1982).
36. R. Navarro, J. Santamaria, and J. Bescos, "Accommodation-dependent model of the human eye with aspherics," J. Opt. Soc. Am. A **2**, 1273 - 1281 (1985), http://www.opticsinfobase.org/abstract.cfm?URI=josaa-2-8-1273.
37. I. Powell, "Lenses for correcting chromatic aberration of the eye," Appl. Opt. **20**, 4152-4155 (1981).
38. Y. Benny, S. Manzanera, P. M. Prieto, E. N. Ribak, and P. Artal, "Wide-angle chromatic aberration corrector for the human eye," J. Opt. Soc. Am. A **24**, 1538-1544 (2007).
39. X. Zhang, A. Bradley, and L. N. Thibos, "Achromatizing the human eye: the problem of chromatic parallax," J. Opt. Soc. Am. A **8**, 686-691 (1991), http://www.opticsinfobase.org/abstract.cfm?URI=josaa-8-4-686.
40. L. N. Thibos, "Calculation of the influence of lateral chromatic aberration on image quality across the visual field," J. Opt. Soc. Am. A **4**, 1673-1680 (1987), http://www.opticsinfobase.org/abstract.cfm?URI=josaa-4-8-1673.
41. X. Zhang, A. Bradley, and L. N. Thibos, "Experimental determination of the chromatic difference of magnification of the human eye and the location of the anterior nodal point," J. Opt. Soc. Am. A **10**, 213-220 (1993), http://www.opticsinfobase.org/abstract.cfm?URI=josaa-10-2-213.
42. M. Rynders, B. Lidkea, W. Chisholm, and L. N. Thibos, "Statistical distribution of foveal transverse chromatic aberration, pupil centration, and angle ψ in a population of young adult eyes," J. Opt. Soc. Am. A **12**, 2348-2357 (1995).

1. Introduction

The use of optical coherence tomography (OCT) [1-8] has revolutionized treatment and monitoring of retinal diseases in everyday clinical settings. Its superb axial resolution, independent from lateral resolution, allows precise *in vivo* visualization and characterization of all the main cellular layers in the human retina. Unfortunately, similarly to other imaging techniques, lateral resolution and, therefore quality of the OCT imaging is reduced by imperfections in the eye's optics. This effect is more evident if one increases the size of the imaging aperture to be greater than 2 mm at the eye's pupil [9]. Improvements in lateral resolution have been demonstrated by incorporation of wavefront correctors in various retinal imaging systems starting with a flood illuminated ophthalmoscope [10] followed by scanning laser ophthalmoscopes [11], and recently into many variations of OCT systems [12-21]. A short overview of different configurations and corrector types implemented in those AO-OCT systems has recently been published by Pircher and Zawadzki [22]. While each of these AO-OCT cameras reduces the degrading impact of the ocular aberrations, full compensation of both low- and high-order aberrations of the eye has not been achieved. This becomes a limiting factor when AO-OCT systems are used in clinical settings, where most patients are known to have moderate amounts of refractive error. Standard methods for refractive error correction, such as placement of trial lenses or a trombone in front of the eye cannot be easily implemented without affecting OCT detection. As a possible solution to this problem, we recently reported [19] a novel "trial lens free" AO design that cascades two DMs for the purpose of extending the correction range (amplitude) and capabilities, compared to the systems using a single wavefront corrector. The performance of our AO subsystem has been evaluated by measuring the quality of the wavefront correction as well as characterizing the corresponding OCT images. This two-DM AO system was integrated into the ultrahigh-resolution (UHR) OCT system (AO-UHR-OCT) presented in this paper.

In UHR-OCT [23], a ~3 μm axial resolution results from the use of an ultra broadband source. The signal-to-noise penalty that occurs due to the wider optical bandwidth in time-domain OCT is waived when an ultra broadband source is used in a Fourier-domain OCT (Fd-OCT) configuration [24,25]. UHR Fd-OCT images with an axial resolution of ~3 μm were first demonstrated in 2004 [26,27]. First attempts to combine UHR-OCT with AO have been reported [13,18], however published retinal images did not demonstrate a clear improvement

#94149 - $15.00 USD Received 24 Mar 2008; revised 16 May 2008; accepted 17 May 2008; published 20 May 2008

compared to standard AO-OCT. In this paper we describe the next generation of our AO-OCT instrumentation where a broader spectral bandwidth light source combined with a custom designed achromatizing lens is used to increase measured axial resolution to ~3.5 μm, without reduction in the lateral resolution and image quality. Results obtained with this improved AO-UHR-OCT system are provided and some performance measures are compared to our previous AO-OCT instrument that had a measured axial resolution of ~6.5 μm. Additionally, benefits of speckle size reduction due to increased light source spectral bandwidths and a method to further decrease speckle contrast [28] are presented and tested.

2. Materials and methods

2.1 AO UHR-OCT instrument

Most of the main components and imaging procedures of our AO-UHR-OCT system have been described in our previous publications on AO-OCT [16,17,19]. Therefore, here we will focus mainly on the new components that make AO-UHR-OCT imaging possible. Briefly, light from a superluminescent diode is split by a 90/10 fiber directional coupler into the reference and sample arms of the OCT system's Michelson interferometer, respectively. The measured light level at the entrance pupil of the subject's eye does not exceed 400 μW. An AO system has been introduced into the OCT sample arm to allow correction of the subject's ocular aberrations. Light back-scattered from the retina is combined with light from the reference arm and the spectral fringes are acquired in the detection channel of the OCT spectrometer. A water cuvette placed in the reference arm approximately matches the chromatic dispersion induced by the human eye in the sample arm; any remaining dispersion mismatch is corrected by Fd-OCT reconstruction software [16]. This system occupies a 5 ft x 6 ft laboratory optical table. The OCT-control unit drives vertical and horizontal scanners with programmable scanning patterns (max of 4° field of view), acquires ~18k lines/s for 50 μs line exposures and displays 32 frames/s with 500 lines/frame of OCT data. An AO-control system operates the AO closed loop correction at a rate at 16 Hz.

The current AO control software allows AO correction for a single DM at a time, *i.e.* while one DM is correcting in a closed loop, the second DM is either in a holding mode (retaining its shape from its previous iterations) or in an inactive mode (flat state). The system operator determines which DM is activated and in which order. The same light source is used for both wavefront sensing and imaging, to permit the OCT data to be saved without interfering with the AO system operation. In the optical design of our AO-OCT sample arm, we used a series of focal telescopes to image the eye's pupil on all key optical components, including vertical and horizontal scanning mirrors, wavefront correctors DM 1 and DM 2, the Hartmann-Shack wavefront sensor and the fiber collimator for light delivery. The magnification factor, γ, between the eye's pupil and the planes where the DMs are situated depends on the physical dimensions of the wavefront correctors. Accordingly, it was 1.51x for the AOptix Bimorph mirror, DM 1 (~10 mm diameter pupil image), and 0.47x for the Boston Micromachines MEMS mirror, DM 2 (~3.125 mm diameter pupil image) based upon the ~ 6.6 mm subject pupil diameter used for imaging. Figure 1 shows a detailed view of the sample arm of the system, including a simplified schematic of the focal telescopes depicting all optically conjugated planes to the eye's pupil and retina.

#94149 - $15.00 USD Received 24 Mar 2008; revised 16 May 2008; accepted 17 May 2008; published 20 May 2008

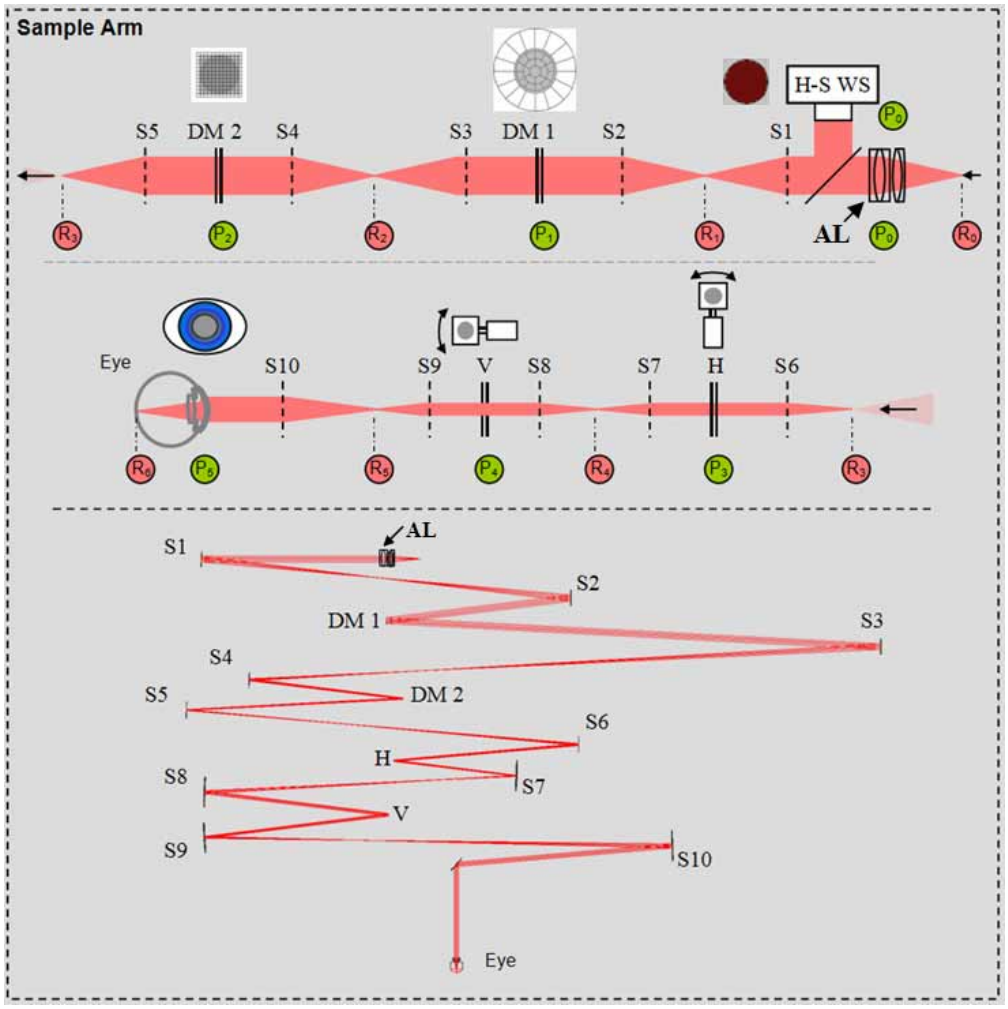

Fig. 1. Upper panel shows unfolded version of schematic of the sample arms of the AO-UHR-OCT instrument. The light travels from left to right in the upper panel. P and R refer to pupil and retinal conjugate planes, respectively; AL – achromatizing lens; S –spherical mirror; V – vertical, H – horizontal scanner. Lower panel shows layout of the sample arm screen shot from system simulation in Zemax. Note the location of the achromatizing lens, which is positioned adjacent to the collimating lens in the pupil conjugate plane, P_0.

The actual layout of the sample arm, as visualized by the optical design program Zemax, which was used to evaluate the optical performance of the AO-UHR-OCT sample arm, is also presented. Note that spherical mirrors are used in all telescopes in this system. Another feature of our 2 DM AO control is the ability to set the AO correction reference focus at any depth within the retina by introducing a given amount of defocus to the H-S centroid reference file, which, in turn, shapes the profile of DM1 accordingly. Once a certain amount of defocus is introduced to DM1, the AO correction is performed the same way as described above, i.e., DM1 is activated first to correct for the lower-order aberrations and then DM2 is activated to correct for the remaining higher-order aberrations, while DM1 is held to the shape of its last iteration. This provides an important research tool as it allows fine adjustment of the focusing plane within the retina without reduction in AO performance, resulting in depth of focus on the order of less than 50 μm, which is only a fraction of the whole retinal thickness. Additional details on our 2DM-AO system components can be found elsewhere [19].

#94149 - $15.00 USD Received 24 Mar 2008; revised 16 May 2008; accepted 17 May 2008; published 20 May 2008

2.2. Chromatic aberrations of the human eye

The human eye suffers from significant chromatic aberrations, due primarily to its watery composition whose refractive index varies with wavelength. The longitudinal (LCA) and transverse (TCA) components of the ocular chromatic aberrations have been extensively studied at visible [29], and more recently near infrared wavelengths [30-32]. LCA and TCA refer to the variation in focus and image size with wavelength, respectively. Numerous achromatizing lenses have been designed based on a zero-power triplet for specific correction of LCA in the human eye [33-36]. By themselves, triplets exhibit substantial TCA when used off axis, and therefore more complex designs (combination of triplets and doublets) have been proposed for improved performance [37, 38]. These designs have proven effective at correcting the eye's LCA, which is largely uniform across eyes and insensitive to field angle. However regardless of the design, similar success has not been achieved with correcting the eye's TCA, which varies across eyes and is highly sensitive to field angle. In some cases, slight misalignment of the achromatizing lens to the eye was found to substantially increase the TCA, well above that with which the eye is endowed. Despite mixed success of the achromatizing lenses to improve visual performance, high-resolution retinal imaging, in particular AO-OCT, represents a potentially more promising application. AO-OCT instruments have several key attributes that reduce the demand on the achromatizing lens. These include a comparatively small field of view, imaging at near-infrared wavelengths, a limiting pupil that is specified by the retina camera rather than the eye, stabilization of the subject's head with a bite-bar stage and forehead rest rather than a chin rest, and raster scanning of the retina using galvanometer scanning mirrors.

While an achromatizing lens has already been suggested for AO-OCT retinal imaging [31], our strategy and results differ on several fronts. First, our design and analysis of the achromatizing lens focuses on the above system attributes specific for retinal imaging rather than general performance characteristics of the lens, as for example for lens tilt and translation errors. While such general analysis is valuable, it is not necessarily applicable to the problems encountered in retinal imaging. Second, our achromatizing lens is designed for placement at the light input of the AO-OCT sample arm. Third, as supportive evidence of the benefit of the achromatizing lens, *in vivo* images of normal and pathologic retina are acquired with AO-OCT and AO-UHR-OCT systems, the latter endowed with an achromatizing lens. To our knowledge, these represent the first such images obtained with this combination.

2.2.1. TCA for retinal imaging

Achromatizing lenses do not correct for TCA of the eye, which can be substantial and can dilute the benefit of the LCA correction by the lens. To determine the extent to which TCA impacts retinal imaging and the conditions under which it can be held at acceptable levels for high-resolution retina cameras, we investigated theoretically the eye's chromatic performance using a reduced eye model. This model was chosen owing to its simplicity and prior validation for studying chromatic effects in the human eye [39-41]. For this model, the nodal point of the eye is located at the center of curvature of the single refractive surface. As shown in Figs. 2(A)-2(D), the sample arm of the AO-OCT camera from Fig. 1 is reduced to its key components that capture the effect of the ocular chromatic aberrations: a point source (fiber tip), collimating lens, achromatizing lens, several conjugate retinal and pupil planes internal to the system, and finally an external exit pupil. All components of the camera are concentric and aligned to the optical axis (OA) of the camera. For this arrangement, degradation of camera performance by tilt and lateral translation of the achromatizing lens relative to the camera's optical axis (as reported in other publications) is not relevant since the achromatizing lens can be aligned accurately and straightforwardly to the camera's axis. The eye's entrance pupil is positioned conjugate to and centered on the camera's exit pupil, a step consistent with standard alignment practice of high-resolution retina cameras. Note that the exit pupil of the camera (in our case 6.6 mm) is smaller than the entrance pupil of the eye (about 8 mm) and therefore represents the limiting pupil of the eye-camera system.

#94149 - $15.00 USD Received 24 Mar 2008; revised 16 May 2008; accepted 17 May 2008; published 20 May 2008

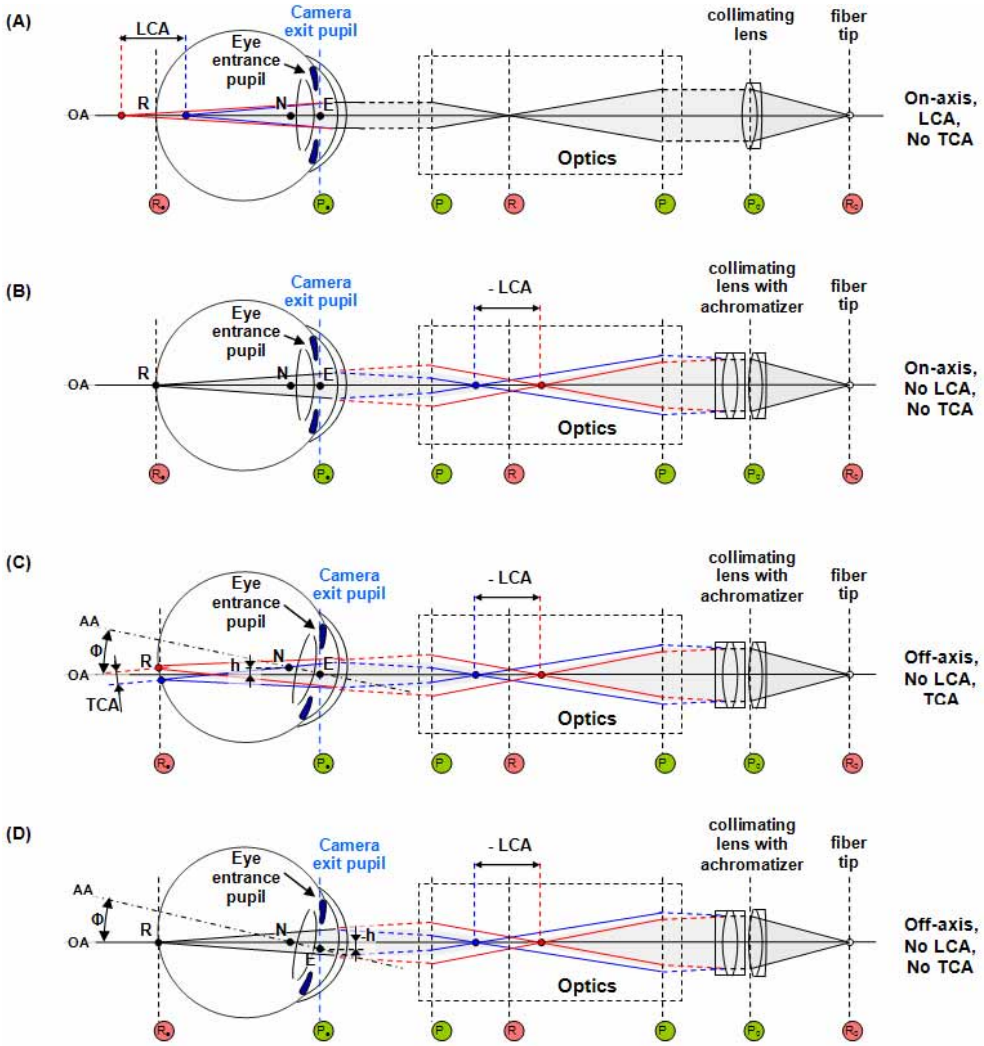

Fig. 2. Eye alignment and use of an achromatizing lens influence the impact of ocular chromatic aberrations on retinal imaging. (a) On-axis imaging without an achromatizing lens is degraded by the eye's LCA. TCA, on the other hand, is zero as the eye's achromatic axis and camera's optical axis are coaligned. (b) LCA is removed by introduction of an achromatizing lens. TCA is again zero as the axes remain coaligned. (c) Off-axis imaging allows view of the peripheral retina, but necessitates rotation of the eye relative to the axis of the camera, in this case by an amount ϕ. LCA of the eye is largely insensitive to rotation, while TCA is not. (d) For off-axis imaging, TCA can be removed by lateral shifting of the eye such that the eye's nodal point once again intersects the camera's optical axis. (key: AA – eye's achromatic axis; OA – camera's optical axis; N – eye's nodal point; E – center of eye's entrance pupil; h – displacement of eye's nodal point from the camera's optical axis; ϕ - rotation of eye about E.)

Important to our analysis is the achromatic axis (AA) of the eye that is defined as the line that intersects the nodal point, *N*, and entrance pupil center, *E*, of the eye. Note that the eye and camera share the same achromatic axis whenever the camera's optical axis passes through the eye's entrance pupil, *E*, and nodal point, *N*. One required condition for this to occur is that the eye's entrance pupil must be centered on the camera's exit pupil, a condition that holds for all of the imaging experiments in this paper. TCA is by definition zero along the achromatic axis and therefore lateral resolution at the retinal point intersected by this axis is dictated entirely be monochromatic aberrations and diffraction. Figure 2(A) depicts the common

#94149 - $15.00 USD Received 24 Mar 2008; revised 16 May 2008; accepted 17 May 2008; published 20 May 2008

retinal imaging scenario (without an achromatizing lens) in which ocular chromatic aberrations cause shorter wavelength light to focus closer and longer wavelength light further away. This causes appreciable LCA (~2 diopters across the visible spectrum). On the other hand, TCA is zero as the achromatic axis of the eye co-aligns with the optical axis of the camera. Insertion of an achromatizing lens [Fig. 2(B)] of equal but opposite LCA to that of the eye brings to focus both short and long wavelength light at the retina. In this case, LCA of the eye-camera system is zero. As the achromatic axis of the eye remains co-aligned to the optical axis of the camera, TCA also remains zero. This scenario illustrates the ideal case in which the longitudinal and transverse chromatic effects are fully corrected. Imaging for this scenario, however, is confined to the patch of retina through which the achromatic axis of the eye passes. Figure 2(C) illustrates the situation in which patches of retina at other retinal eccentricities are imaged. In this case, the eye is rotated by ϕ about *E*, while the eye's pupil remains centered on the camera's exit pupil (which follows standard practice for aligning AO-based cameras). In Fig. 2(B), the fiber tip is imaged to different axial locations inside the camera depending on the wavelength. This effect, while inconsequential when the optical axis of the camera and achromatic axis of the eye are co-aligned, leads to chromatic parallax when the two are not. This is the scenario depicted in Fig. 2(C) and shows the impact of lateral displacement of the eye nodal point relative to the optical axis of the camera. As described by Zhang, *et al*., (see Eq. (2)) [39], the resulting TCA in radians for this scenario is

$$TCA = (F_a - F_b)\, h, \tag{1}$$

where F_a and F_b are the dioptric powers of the achromatizing lens for the extreme wavelengths *a* and *b* of the source spectrum. *h* is the lateral displacement of the nodal point from the optical axis of the camera and is expressed as

$$h = |NE| \tan(\phi), \tag{2}$$

|NE| is the geometrical distance between the nodal point, *N*, and center of the exit pupil, *E*, and ϕ is the rotation of the eye about *E*. Finally, as shown by Fig. 2(D), chromatic-aberration-free imaging can be recovered if rotation of the eye, ϕ, is accompanied by sufficient lateral translation, *h*, such that the nodal point shifts back onto the camera's optical axis. Note that re-positioning the nodal point requires the camera's exit pupil (6.6 mm for our camera) to be smaller than the eye's entrance pupil (>8 mm for our subjects). Naturally, there is a limit to how much the eye can rotate before the pupil of the eye apodizes the beam.

In summary, Fig. 2(C) conveys the two primary contributors of TCA for retinal imaging: (1) errors in the lateral positioning of the eye, *h*, relative to the optical axis of the retina camera and (2) off-axis imaging, ϕ, *i.e.*, imaging away from the achromatic axis of the eye. To theoretically address the impact of each on camera performance, we quantified the magnitude of TCA using the reduced eye model, Eqs. (1) and (2), and ocular dispersion at near-infrared wavelengths. Several near-infrared bands were chosen that correspond to common OCT light sources. Additionally, we quantified the range of eye rotation over which TCA can be zeroed with appropriate lateral shift of the eye, typical pupil sizes, and *a priori* knowledge of the nodal point location.

2.2.2. Correct LCA with a customized achromatizing lens

Similar to the design strategy of Fernandez, *et al*. [31], we simulated in Zemax software the chromatic effects of the achromatizing lens and employed the Navarro eye model [36] with Atchinson and Smith's extension to the near infrared region [32]. In contrast to Fernandez, *et al.*, the performance of the achromatizing lens was optimized in the actual model of the sample arm of an AO-UHR-OCT imaging system (as shown by the lower panel of Fig. 1). The lens was specifically designed for placement at the entrance of the sample arm and adjacent to the collimating objective. This position prevents back reflections from the flat surfaces of the achromatizing lens from entering the SH wavefront sensor, which may otherwise occur if placed between the subject's eye and sensor. Figure 3 shows a schematic of the achromatizing lens and collimating objective.

#94149 - $15.00 USD Received 24 Mar 2008; revised 16 May 2008; accepted 17 May 2008; published 20 May 2008

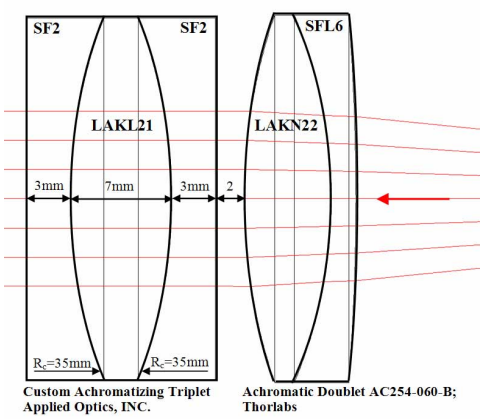

Fig. 3. Design of collimating doublet (achromatizing lens + commercial achromat) used at the entrance of the AO-UHR-OCT system. The achromatizing lens is a zero-power triplet. Red arrow indicates direction of the light emitted from the fiber (to the right of the doublet).

The achromatizing lens is inserted into the same optomechanical mount tube as the collimating objective (commercial achromat). This assures that the achromatizing lens is well centered on the system's optical axis and pupil. Another advantage of this design is that no extra pupil plane is required in the imaging system, thereby allowing straightforward integration into existing instruments with only minor modifications. The achromatizing lens design was based on simulation in Zemax to minimize LCA over the wavelengths of our light source. This was accomplished by varying curvature, thickness and optical material used in fabrication of the achromatizing lens. To minimize cost, only stock optical glass was considered

2.3. Speckle reduction

Speckle noise is intrinsic to OCT due to its coherent detection scheme. The lateral dimension of the average speckle is governed by the numerical aperture of the imaging system and is approximately equal to the diffraction-limited spot size. The axial dimension of speckle, on the other hand, is governed by the source spectrum and is approximately equal to the axial coherence length of the source. The use of the maximum possible NA with a pupil size of 6-7 mm of AO-based retinal imaging systems make them naturally fitted to reduce lateral speckle size. Additionally, the implementation of ultra broadband light sources in UHR-OCT showed a clear improvement in reducing degradating effects of speckles on image quality. Therefore, an AO-UHR-OCT instrument offers the best possible speckle size reduction in lateral and transverse directions, improving the visibility of retinal features. A greater reduction of speckle appearance would still be of interest. Unfortunately we are at the limit of the accessible NA of the imaging system because the pupil cannot be dilated much further. A possible increase of the spectral bandwidth is still possible, however it requires more costly light sources, and detectors, and a more complex optical design to correct the eye's chromatic aberrations. As already pointed out this design should not be limited to LCA alone, but must also compensate for TCA. However there have been recent reports on simple methods of speckle contrast reduction by averaging of multiple OCT B-scans [28]. This method is not feasible for volumetric imaging, with the acquisition speed of our current system, but it can be applied to single location B-scans. In the speckle reduction procedure presented in this paper we used sets of B-scans acquired over the same 0.5 or 1 mm area of the retina. These data were post-processed beginning with frame registration [19]. Then, from a set of 100 or 200 frames we choose 10 frames that have minimum motion artifacts and that showed similar retinal structures (this is necessary because vertical eye motion shifts our B-scans to different retinal locations). These frames are then averaged; each pixel value is the mean intensity from all frames, to create one frame.

#94149 - $15.00 USD Received 24 Mar 2008; revised 16 May 2008; accepted 17 May 2008; published 20 May 2008

3. Results and discussion

3.1. Theoretical results for TCA and LCA

A reduced model eye was used to predict the magnitude of TCA for three retinal imaging scenarios. For off-axis imaging, Fig. 4 shows the range of eye rotation, $\pm\phi$, over which TCA can be zeroed simply by re-positioning the eye until its nodal point coincides with the camera's optical axis. This scenario is depicted schematically in Fig. 2(D). As evident in Fig. 4, the amount of allowable rotation depends strongly on the camera's exit pupil diameter, with a larger camera pupil reducing the allowable rotation. For the AO-UHR-OCT system described here, which has a 6.6 mm exit pupil, TCA-free imaging is predicted over a ±9.2° rotation. Interestingly, conventional OCT (without AO) typically has a camera exit pupil of about 1.5 mm, which allows a much larger ± 33° rotation. Of course this strategy for zeroing the TCA relies on the premise that the location of the nodal point is known, which in actual imaging situations is rarely the case. Nevertheless, our theoretical results with the reduced eye reveal that proper alignment of the eye to the camera enables TCA-free imaging of the retina from the fovea to almost the optic disc (15° retinal eccentricity) even for relatively large camera pupils.

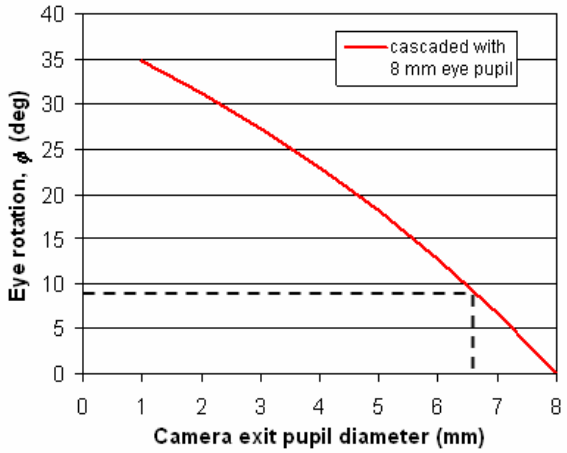

Fig. 4. Range of eye rotation, $\pm\phi$, over which TCA can be zeroed simply by re-positioning the eye until its nodal point conincides with the camera's optical axis. Maximum rotation is reached when the eye's pupil begins to occlude the camera's exit pupil. Diameter of the eye's pupil was set to 8 mm. Separation of the nodal point and entrance pupil of the eye is assumed to be 4 mm [40]. Dashed line highlights maximum rotation predicted for the AO-UHR-OCT system described here (6.6 mm pupil).

Without knowledge of the nodal point location, high-resolution retina cameras – such as the one described here – rely on an alignment procedure in which the entrance pupil of the eye is simply centered on the exit pupil of the camera. This begs the question then as to how much TCA is induced by centering the pupils for off-axis imaging (as for example the scenario depicted in Fig. 2(C)) and furthermore how much error in the lateral alignment of the eye to the camera can be tolerated. For the latter question, Fig. 5(left) shows the predicted TCA for lateral displacement of the eye's nodal point from the camera's optical axis. The figure shows that larger displacements as well as wider source spectra lead to larger TCA. Empirically, we have observed that use of a pupil camera and bite-bar stage permits accurate positioning of the subject's pupil to within about ± 0.5 mm. The achromatic axis associated with a given patch of retina is defined by a line that intersects the patch of retina and nodal point of the eye. Assuming momentarily that this achromatic axis passes through the center of the eye's entrance pupil (h = 0), a ± 0.5 mm error in Fig. 5(left) corresponds to a maximum TCA of 0.7, 1.6, and 2.3 μm for the 50 nm (SLD 371-HP), 112 nm (SLD T840-HP), and 140 nm

#94149 - $15.00 USD Received 24 Mar 2008; revised 16 May 2008; accepted 17 May 2008; published 20 May 2008

(Ti:Sapphire) light sources, respectively. These TCA values are all noticeably smaller than the 3.5 μm lateral resolution we can achieve with the AO system and therefore should have little impact on overall image quality. However, we do not know if the achromatic axis, associated with a particular patch of retina, intersects the center of the entrance pupil for the subjects we imaged in this paper. Rynder, *et al.*, [42] sheds some insight into this at least for the foveal region. They measured the separation, *h*, for the foveal achromatic axis in a population of young adult eyes. The average eye was found to be free of TCA at the fovea ($\langle h \rangle = 0$). The average magnitude, $|h|$, however was <0.5 mm and ranged from 0.02 to 1.21 mm. Combining the 0.5 mm average magnitude with our ± 0.5 mm alignment accuracy suggests an actual lateral displacement, *h*, that is likely no larger than 1 mm, which corresponds to 3.2 μm for our SLD T840-HP source (UHR-AO-OCT). This is still less than the 3.5 μm lateral resolution of our AO, but likely large enough to cause degradation of image quality.

While careful attention to pupil alignment (as was done here) appears to keep TCA at acceptable levels, many types of retina cameras are not designed with such accuracy. This may be particularly fitting of most OCT instruments (non-AO) that use small beam diameters and rely on a chin rest rather than bite-bar stage. For these instruments, positioning errors of 2 and 3 mm is probably common and correspond to TCA values that can approach 15 μm, especially when broadband light sources are used.

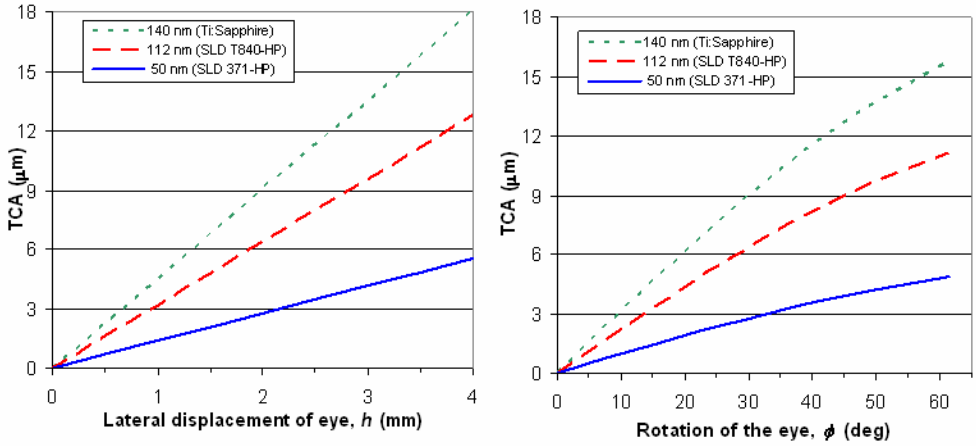

Fig. 5. Modeling of TCA as a function of (left) lateral misalignment of the eye, *h*, and (right) off-axis imaging, ϕ. (Left) TCA is plotted as a function of lateral displacement of the eye's nodal point relative to the optical axis of the retina camera. (Right) TCA is plotted as a function of eye rotation (defined as the angle between the camera's optical axis and the eye's achromatic axis). The eye's entrance pupil remains centered on the camera's optical axis, which is consistent with our experimental alignment protocol. Three near-infrared bands were chosen that correspond to specific OCT light sources.

Figure 5 (right) shows the predicted TCA for off-axis imaging when the eye's entrance pupil remains centered on the camera's exit pupil. The figure shows that larger rotations as well as wider source spectra lead to larger TCA. As an example for our SLD T840-HP source (UHR-AO-OCT), the TCA remains below 3.5 μm up to ± 16° of rotation. This suggests that much of the retina from the fovea up to about the optic disc can be imaged with this source with relatively small TCA. The 50 nm source will allow even larger rotation (± 39°), while the 140 nm less (± 11°). Figure 5(right) assumes the eye's entrance pupil is centered on the camera's exit pupil. However, if the two could be offset using the alignment strategy investigated in Fig. 4, TCA could be reduced further and permit larger rotations. Of course this requires that the location of the eye's nodal point is known or can be estimated.

Next, we evaluated the performance of our achromatizing lens to correct the LCA of the eye using the commercial ray trace software, Zemax. Figure 6 shows the effectiveness of the

#94149 - $15.00 USD Received 24 Mar 2008; revised 16 May 2008; accepted 17 May 2008; published 20 May 2008

achromatizing lens across the 50 and 112 nm bandwidths of the SLD 371-HP and SLD T840-HP light sources.

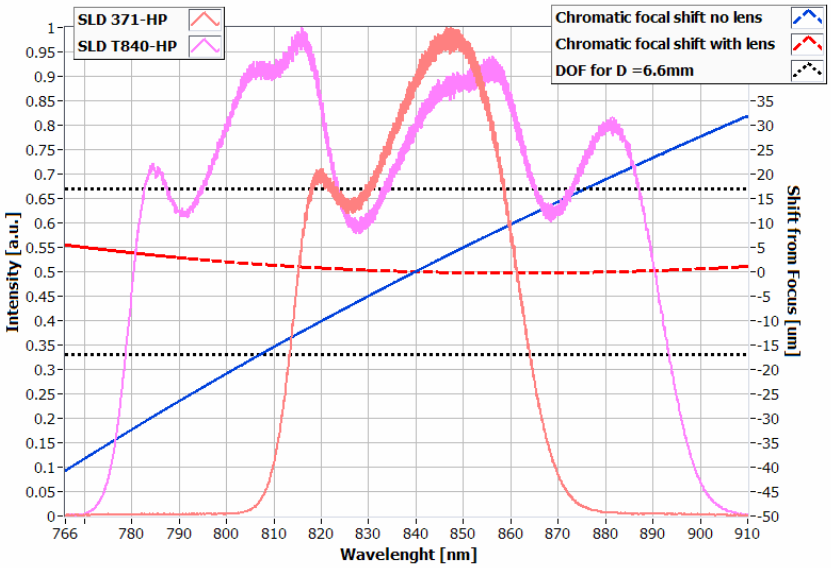

Fig. 6. (Left axis) Spectral distribution of two light sources used to evaluate the performance of our custom achromatizing lens. (Right axis) Chromatic focal shift at the retina is predicted using a Zemax model of the eye and retina camera combination with and without the achromatizing lens. Depth of focus expected for diffraction-limited performance through a 6.6 mm pupil is also shown.

Figure 6 also shows the depth of focus for diffraction-limited performance through a 6.6 mm pupil (defined by DOF $\approx 6\lambda(f/D)^2 = 33$ μm, where f = 16.7 mm) together with the spectral profiles of two light sources used to evaluate the system. The two sources included an SLD 371-HP, which was previously reported for AO-OCT ($\Delta\lambda = 50$ nm, $\lambda_0 = 841$nm; $P_{out} = 8$ mW) and an ultra broad bandwidth Broadlighter T840-HP used in AO-UHR-OCT ($\Delta\lambda = 112$ nm; $\lambda_0 = 836$ nm; $P_{out} = 16$ mW). These are experimental data as measured at the OCT detection spectrometer (light from the reference arm only). High frequency modulations superimposed on the light source spectra are due to "coherence noise" terms (multiple back-reflections in the reference arm). Note that for the Broadlighter T840-HP, LCA of the eye causes wavelengths at the edges of source spectrum to focus well outside the depth of focus for a 6.6 mm pupil, confirming that LCA correction is required for diffraction-limited imaging.

3.2. Experimental results

To date more than 20 individuals (including healthy and diseased retinas) have been imaged with our UHR-AO-OCT. A forehead rest and bite bar, together with external fixation light, were used to minimize head and eye motion. Before each imaging session, the subject's eyes were dilated and cyclopleged.

3.2.1. AO-OCT vs. AO-UHR-OCT

To test the improvement achieved with our new UHR-AO-OCT system two light sources (both from SUPERLUM LTD.) have been used consecutively. First we used the previously reported SLD 371-HP and then the Broadlighter T840-HP. The same detection arm spectrometer setup was used for both light sources. Only 1024 of 2048 elements of the Atmel line scan CCD camera were active during SLD-371 operation while all 2048 pixels were active for the T840-HP Broadlighter. The coherence length of both light sources was determined *in vivo* from specular reflection in the center of the fovea [26] as measured in our

#94149 - $15.00 USD Received 24 Mar 2008; revised 16 May 2008; accepted 17 May 2008; published 20 May 2008

AO-OCT instrument. The coherence function for both light sources is plotted in Fig. 7; the measured coherence length in tissue (n=1.38) after dispersion compensation was ~6.5 μm for the 371-HP SLD and ~3.5 μm for the Broadlighter T840-HP.

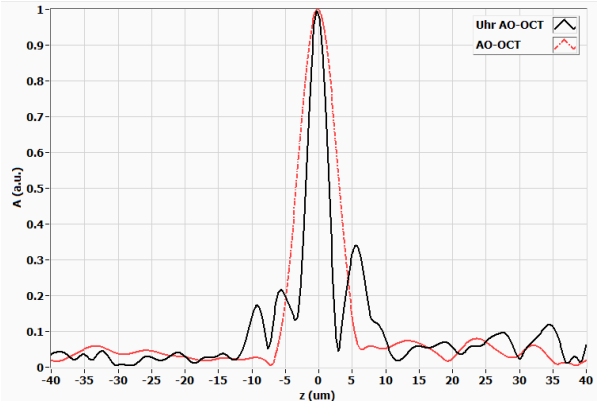

Fig. 7. Coherence function obtained from a reflective spot in the fovea. The measured coherence length in tissue (n=1.38) after dispersion compensation was ~6.5 μm for the 371-HP SLD and ~3.5 μm for the Broadlighter T840-HP.

To illustrate the benefits of increased spectral bandwidth on AO-OCT images, Fig. 8 shows two videos acquired with the same AO-OCT system over the same retinal location (4.5° nasal retina (NR)) with AO focus set on the photoreceptor layers. The only difference between these two B-scans is the spectral bandwidth of SLDs used for imaging.

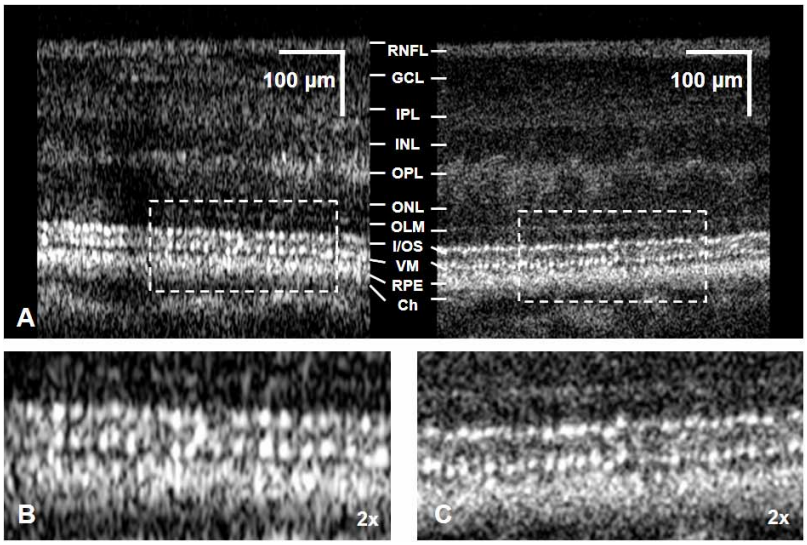

Fig. 8. Comparison of AO-OCT vs. AO-UHR-OCT system performance. A. (4.58 MB) Real-time movie of the in-vivo retina acquired at 4.5° NR eccentricity of the same 35-year-old volunteer (500 A-scans over line of 0.5 mm) by an AO-OCT system with 6.5 μm (left) and AO-UHR-OCT system with 3.5 μm axial resolution (right). AO focus was set on photoreceptor layers. Dashed rectangles correspond to the magnified regions shown in panels B and C. B. Two-fold enlargement of the photoreceptor layer acquired with AO-OCT (left image on panel A). C. Two-fold enlargement of the photoreceptor layer acquired with AO-UHR-OCT (right image on panel A). Retinal Nerve Fiber Layer (RNFL), Ganglion Cell Layer (GCL), Inner Plexiform Layer (IPL), Inner Nuclear Layer (INL), Outer Plexiform Layer (OPL), Fibers of Henle with Outer Nuclear Layer (ONL), Outer Limiting Membrane (OLM), Inner / Outer Segment Junction (I/OS), Verhoeff's Membrane (VM) created by end tips of cone photoreceptor outer segments, Retinal Pigment Epithelium (RPE), and Choriocapillaris and Choroid (Ch).

#94149 - $15.00 USD Received 24 Mar 2008; revised 16 May 2008; accepted 17 May 2008; published 20 May 2008

One image was acquired with our "old" SLD (371-HP with ~6.5 μm axial resolution) and the second was acquired with a broadlighter SLD (T840-HP with ~3.5 μm axial resolution). In addition to a clear improvement in axial resolution, a change can be observed in the thickness at the photoreceptor layer junctions that act as reflecting surfaces; namely (I/OS) and Verhoeff's Membrane (VM - end tips of cone photoreceptors outer segments). The difference in speckle size between the two images seems to have an even bigger effect on visibility of retinal features. One may have the impression that both images have different lateral resolution; however, based on AO system data both images have a similar lateral resolution, on the order of ~3.5 μm (at the photoreceptor layers). This is a clear example of the negative effect that speckle has on the ability to visualize microscopic retinal structures. By playing movies in Fig. 8 an even further reduction of speckles can be observed, due to the temporal averaging of speckle fields by our visual system. A similar effect can be obtained by averaging multiple frames acquired over the same region. We will test this method to further reduce the degrading effect of speckles in the following examples. The names of the retinal layers shown in Fig. 8 are similar to those introduced in our previous work [16].

3.2.2. AO-UHR-OCT with vs. without achromatizing lens

To illustrate the benefit of our achromatizing lens for AO-UHR OCT imaging, Fig. 9 shows two B-scans acquired with the same AO-OCT system over the same retinal location (4.5° nasal retina (NR)) with AO focus at the photoreceptor layers. B-scan acquisition differed only in terms of whether the achromatizing lens was present or absent in the sample channel.

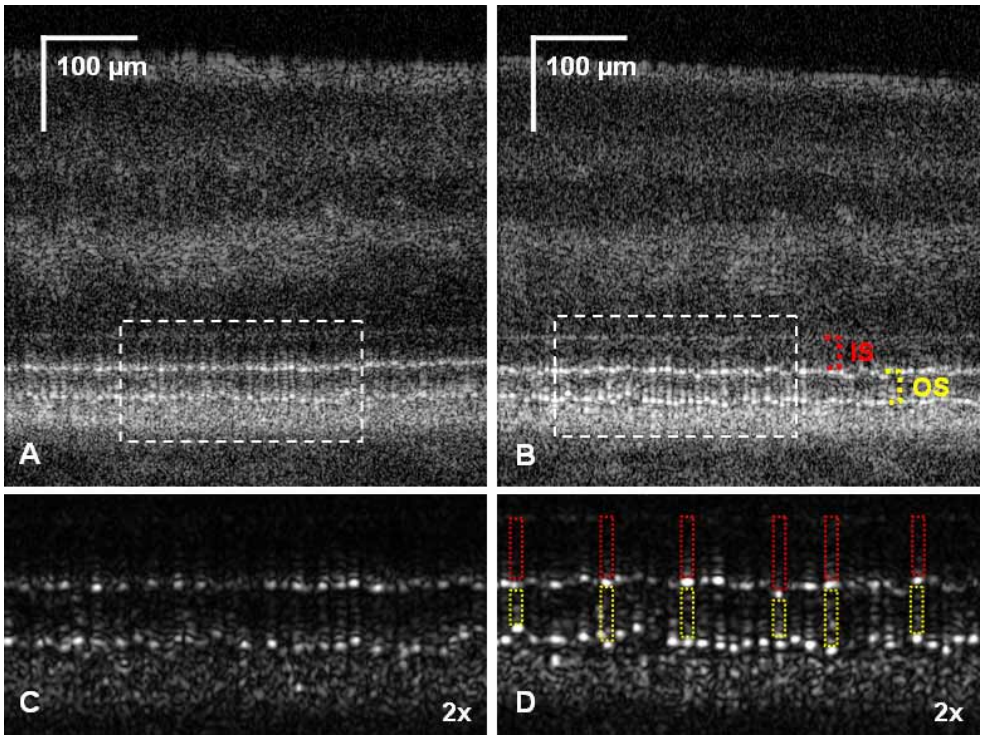

Fig. 9. Comparison of AO-UHR-OCT with and without the achromatizing lens. B-scan acquired at 4.5° NR eccentricity of the same 33-year-old volunteer (500 A-scans correspond to 0.5 mm) by an AO- UHR-OCT system without achromatizing lens (A) and with achromatizing lens (B). AO focus was set on the photoreceptor layer. (C.) Two-fold enlargement of the photoreceptor layer acquired by AO-UHR-OCT without achromatizing lens (linear intensity scale). (D.) Two-fold enlargement of the photoreceptor layer acquired by AO-UHR-OCT with achromatizing lens (linear intensity scale). Photoreceptor Inner Segment (IS), Photoreceptor Outer Segment (OS). Dashed red rectangles show examples of cone photoreceptors inner segments. Dashed yellow rectangles show examples of cone photoreceptors outer segments.

#94149 - $15.00 USD Received 24 Mar 2008; revised 16 May 2008; accepted 17 May 2008; published 20 May 2008

In addition to increased intensity of the photoreceptor layers seen on the B-scan acquired by AO-UHR-OCT with the achromatizing lens (both images are shown using the same intensity scale) an improvement in lateral resolution can be observed. This results in better separation of single photoreceptors as seen on a magnified linear intensity scale of the B-scans in Figs. 9(C) and 9(D). No visible difference in speckle size or axial resolution can be observed. This is a clear example of the negative effect that LCA has on the image quality. Note that one can easily match pairs of bright spots created by light reflected within single cone photoreceptors at the Inner/Outer segment junction and Verhoeff's membrane. This potentially allows length measurement of single photoreceptor inner and outer segments. Intensity on Figs. 8 and 9 logarithmic scale differ due to use of different maximum values used on intensity scale (more pixels are saturated on Fig. 8).

3.2.2. Speckle reduction by multiple B-scan Averaging

Three examples of AO-UHR-OCT image enhancement obtained by applying multiple frames averaging are presented. The first case illustrates the result of this procedure with the corresponding real-time movie acquired at 9° S (superior) 4.5° NR eccentricity.

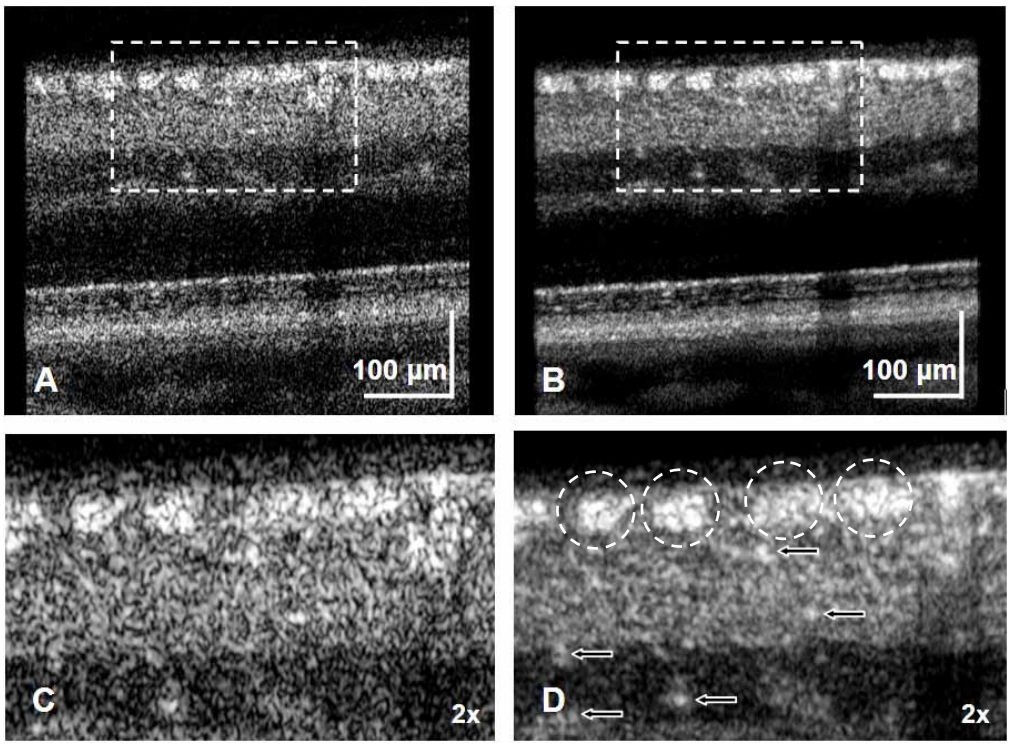

Fig. 10. Comparison of single frame vs. average frame images obtained with AO-UHR-OCT system. AO focus was set on inner retina layers. A. (2.5 MB) Real-time movie acquired with AO-UHR-OCT at 9° S 4.5° NR eccentricity of healthy 55-year-old volunteer (500 A-scans over line of 0.5 mm). Dashed rectangle corresponds to the magnified region shown in panel C. (10 MB version) B. An average of 10 AO-UHR-OCT frames from movie in the panel A. Dashed rectangle corresponds to the magnified region showed in panel D. C. Two-fold enlargement of the single frame of inner retina acquired with AO-UHR-OCT (panel A). D. Two-fold enlargement of the inner retina region from averaged frame (panel B). Note improved visibility of retinal microscopic retinal features on panel D if compared to panel C. Arrows indicate location of micro capillaries in the inner retina. Dashed circles indicate location of the nerve fiber bundles.

In this case our AO sub-system was focused on inner retinal layers (increased sensitivity in RNFL, GCL and IPL). Note that even for this large eccentricity no clear effect of TCA on image lateral resolution or intensity can be observed. Clear reduction in speckle contrast can

#94149 - $15.00 USD Received 24 Mar 2008; revised 16 May 2008; accepted 17 May 2008; published 20 May 2008

be observed between two images after averaging.. This results in increased contrast between RNFL bundles and some capillaries. Granulated structures within inner retinal layers are visible as well. Unfortunately, due to the way this image was created, we cannot definitively correlate these structures with retinal cells. However their location and preservation after speckle averaging suggest that these are real scattering centers lying within retinal layers. Additionally frame averaging increases system sensitivity (ability to see structures with lower reflectance), which is especially important in the context of imaging diseased and elderly eyes which generally appear dimmer due to stronger light absorption and scattering by the ocular media. As background to AO-UHR-OCT imaging in clinical settings, it should be noted that in all AO-based imaging instruments, the image quality is reduced when imaging older or diseased eyes. This is due to a combination of reduced clarity of ocular media, (increased light scattering and absorption) as well as increased ocular aberrations. In many cases the image intensity and resolution are reduced, making it harder to implement AO based cameras in clinical settings where most subjects are either elderly or have eye disease. The next two examples of AO-UHR-OCT imaging in clinical settings presented below are special cases. Namely, image quality and visible retinal features visible on B-scans allowed better diagnosis of retinal conditions than was possible with standard clinical imaging systems. Figure 11 represents micro-traction in the center of the fovea, which due to its small size was not correctly diagnosed using other clinical imaging modalities including commercial Fd-OCT and fundus photography.

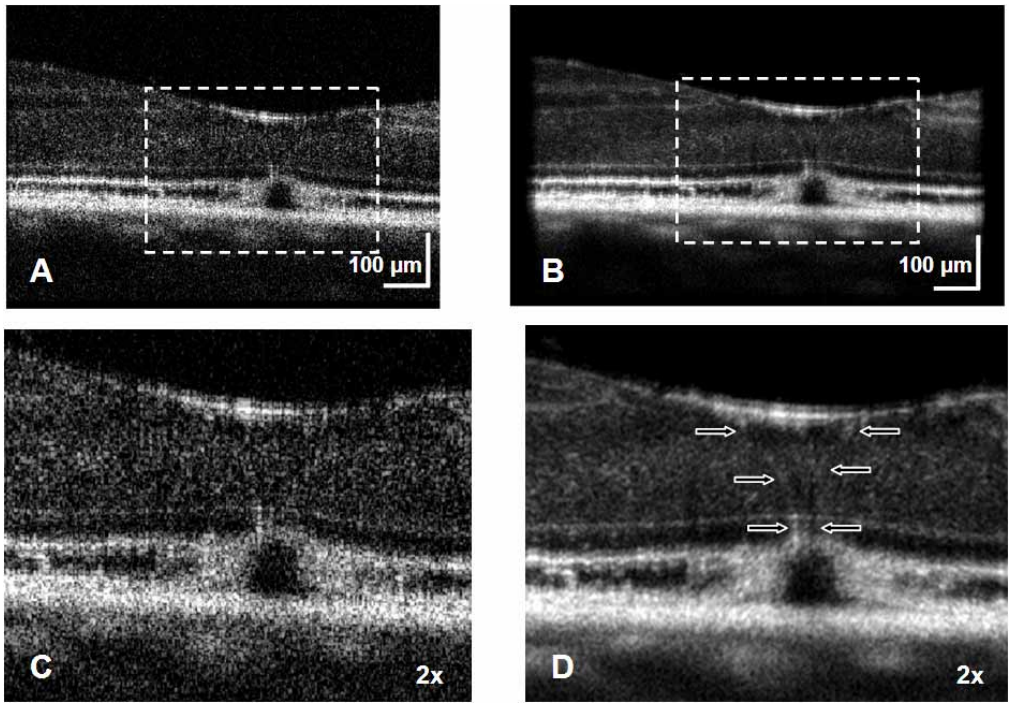

Fig. 11. Comparison of single frame vs. average frame images obtained with an AO-UHR-OCT system. AO focus was set on the ONL. A. (1.6 MB) Real-time movie acquired with AO-UHR-OCT at the fovea of a 65-year-old subject (1000 A-scans over line of 1 mm). Dashed rectangle corresponds to the magnified region showed in panel C. (6.6 MB version) B. An average of 10 AO-UHR-OCT frames from the movie in panel A. Dashed rectangle corresponds to the magnified region shown in panel D. C. Two- fold enlargement of the single frame acquired with AO-UHR-OCT(panel A). D. Two-fold enlargement of the averaged frame (panel B). Arrows indicate probable location of the cells still attached to shrinking vitreous that pull the outer retina outward.

As in Fig. 10, a real time movie, acquired over the foveal region, is presented in Fig. 11 to compare image quality for single and averaged frames. Here, again, improvement in speckle

#94149 - $15.00 USD Received 24 Mar 2008; revised 16 May 2008; accepted 17 May 2008; published 20 May 2008

reduction and sensitivity can be observed, if compared to the single-frame image, permitting insight into retinal structures on a microscopic level. Magnified image allows insight into the structural disruptions associated with retinal detachments caused by shrinking vitreous. This indicates that AO-UHR-OCT may allow monitoring of microscopic structural disruptions associated many retinal diseases.

Figure 12 represents a case of micro-scotoma (small blind spot close to fovea) that could not be explained by any standard imaging modality. It is evident however from AO-UHR-OCT that structural disruptions in the outer nuclear layer extending to the photoreceptor layers are good candidates to account for the reduction in vision reported by this subject. The benefits of averaging multiple frames for improved visualization of retinal structures is evident.

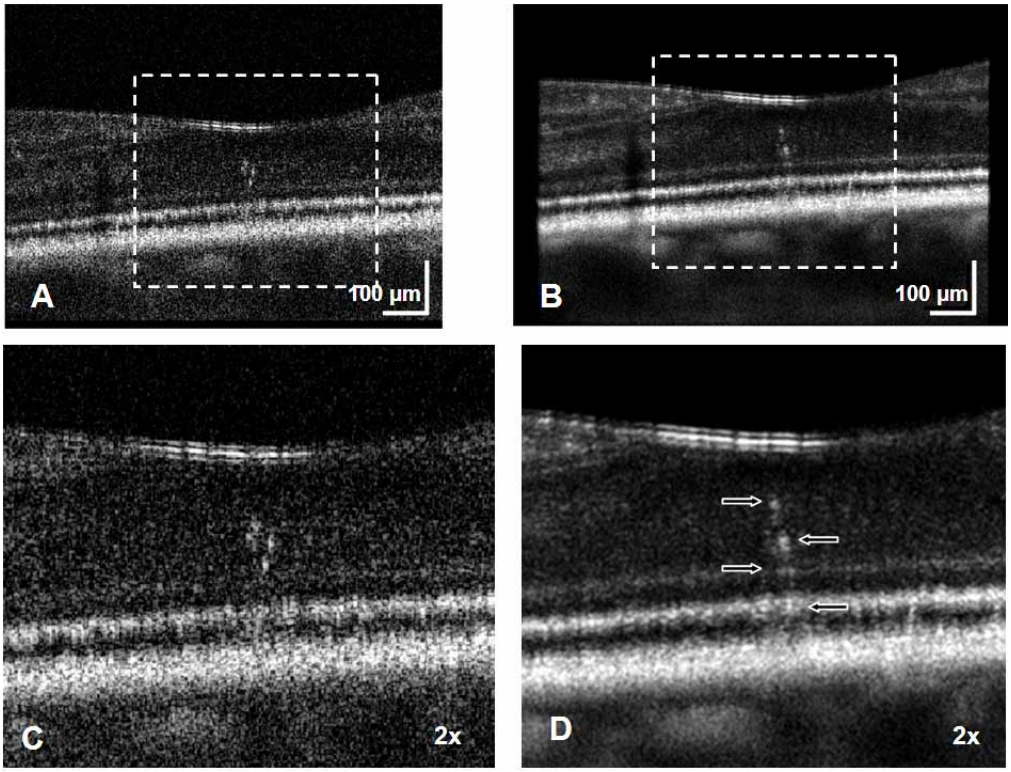

Fig. 12. Comparison of single frame vs. average frame images obtained with AO-UHR-OCT system. AO focus was set on the ONL. A. (1.6 MB) Real-time movie acquired with AO-UHR-OCT at the fovea of 55-year-old subject (1000 A-scans over line of 1 mm). Dashed rectangle corresponds to the magnified region shown in panel C. (6.6 MB version) B. An average of 10 AO-UHR-OCT frames from movie in the panel A. Dashed rectangle corresponds to the magnified region presented in panel D. C. Two-fold enlargement of the single frame acquired with AO-UHR-OCT (panel A). D. Two-fold enlargement of the averaged frame (panel B). Arrows indicate location of the scattering structures lying within the ONL that are probably responsible for the micro scotoma.

These examples demonstrate that speckle reduction by AO-UHR-OCT frame averaging may have an important role in displaying and diagnosing retinal diseases with AO-OCT instrumentation.

4. Conclusions

We have developed an improved AO-OCT system and evaluated its performance for in vivo imaging of normal and pathologic retina. This instrument was used to image the retina in several subjects with isotropic 3.5 μm^3 volumetric resolution. A custom achromatizing lens

#94149 - $15.00 USD Received 24 Mar 2008; revised 16 May 2008; accepted 17 May 2008; published 20 May 2008

was developed for correction of the eye's LCA across the near infrared wavelengths at which the ultra broadband light source operated. Because the achromatizing lens does not correct for TCA induced by the eye, we theoretically investigated the two primary contributors of TCA for retinal imaging: (1) errors in the lateral positioning of the eye and (2) off-axis imaging. TCA was predicted to be relatively small for the imaging conditions in which our AO-UHR-OCT instrument was used.

Diffraction-limited lateral resolution was achieved by cascading two wavefront correctors, a large stroke bimorph DM for correction of large-magnitude, low-order aberrations and a high fidelity MEMS DM for correction of low-magnitude, high-order aberrations. An added benefit of the broadband light source is the reduction of speckle size in the axial dimension. Additionally, B-scan averaging resulted in further reduction of the speckle contrast and enhancement of image sensitivity. As a result, B-scans are easier to interpret. Moreover microscopic scattering structures, that are not speckle noise, lying within retinal layers could be observed. Finally, two examples of AO-UHR-OCT imaging of diseased retinas in clinical settings demonstrated better diagnosis of disease.

Acknowledgments

We thank R. Daniel Ferguson from Physical Sciences Inc. for his input on achromatizing lens design. We gratefully acknowledge the contributions of Steven M. Jones, Julia W. Evans, Diana Chen and Scot S. Olivier from the Lawrence Livermore National Laboratory for providing AO support. Help from Joseph A. Izatt from the Department of Biomedical Engineering, Duke University Durham, NC. and Bioptigen Inc. Durham, NC with providing OCT data acquisition software is appreciated. This research was supported by the National Eye Institute (5R01 EY 014743 and 1R01 EY018339). This work was also supported, in part, by the National Science Foundation Science and Technology Center for Adaptive Optics, managed by the University of California at Santa Cruz under cooperative agreement No. AST-9876783.

#94149 - $15.00 USD Received 24 Mar 2008; revised 16 May 2008; accepted 17 May 2008; published 20 May 2008